JOURNAL OF SOLID STATE CHEMISTRY

Volume 179, Number 4, April 2006

CONTENTS

Regular Articles

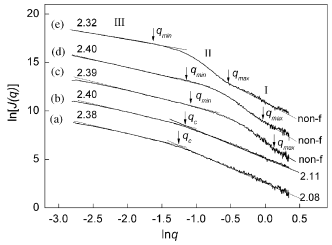

SAXS technique has been employed to study the microstructure evolution of zirconia nanoparticles during the calcination at moderate temperature. Assisted by the analyses of TEM and XRD, SAXS study provides a comprehensive and quantitative characterization of the structural evolution on the nanometer scales.

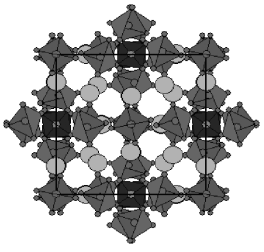

Crystal structure of $Sr_6B(PO_4)_5$ determined by single-crystal X-ray diffraction, structure viewed along [1 0 0] direction.

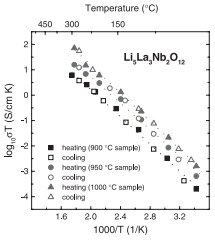

Arrhenius plot of the total (bulk + grain boundary) lithium ion conductivity of $Li_5La_3Nb_2O_{12}$ prepared at three different temperatures, and sample prepared at 1000 °C shows higher electrical conductivity than those prepared at 900 and 950 °C over the investigated temperature range.

Regular Articles—Continued

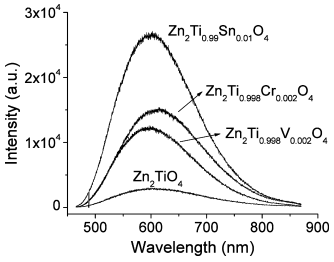

Photoluminescence spectra of disordered Zn_2TiO_4, undoped and doped with Cr^{3+} or Sn^{4+} or V^{5+}.

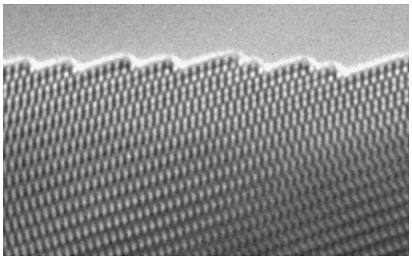

Highly crystalline La_2O_3 formed by electron beam induced in situ transformation.

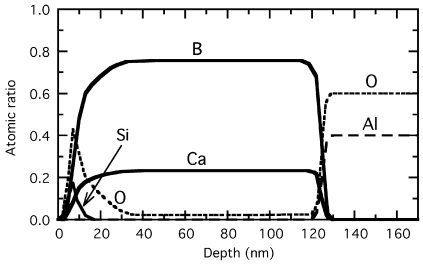

Depth profile of atomic ratio obtained by RBS/NRA method for the CaB_3 film grown on the $Al_2O_3(0001)$ substrate.

NMR study of the order–disorder phase transitions of $KHCO_3$ and $KDCO_3$ single crystals
Ae Ran Lim and Se-Young Jeong
Page 1009

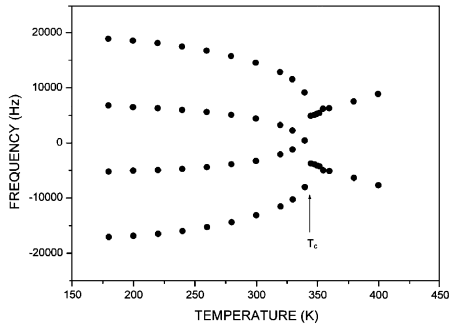

^{2}D NMR spectrum below and above T_C in $KDCO_3$ crystals.

Synthesis and crystal structures of La_3MgBi_5 and $LaLiBi_2$
Da-Chun Pan, Zhong-Ming Sun and Jiang-Gao Mao
Page 1016

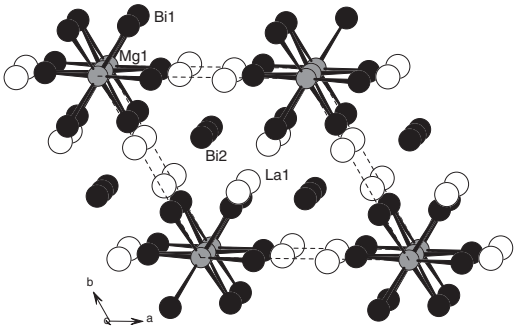

View of the structure of La_3MgBi_5 down the *c*-axis. The Mg, La and Bi atoms are drawn as gray, white and black circles, respectively.

New insight into the symmetry and the structure of the double perovskites Ba_2LnNbO_6 (*Ln* = lanthanides and Y)
W.T. Fu and D.J.W. IJdo
Page 1022

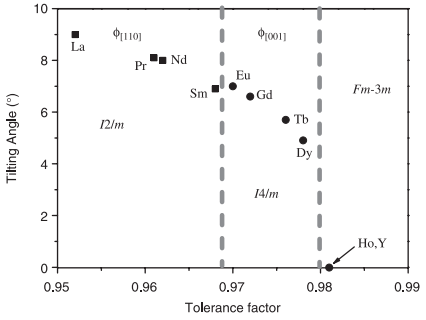

Tilting angles in Ba_2LnNbO_6 (*Ln* = La, Pr, Nd, Sm, Eu, Gd, Tb, Dy, Ho, and Y) as the function of the tolerance factor *t*.

Low-temperature synthesis and structure characterization of the serials $Y_{2-\delta}Bi_\delta Sn_2O_7$ ($\delta = 0$–2.0) nanocrystals
KunWei Li, TingTing Zhang, Hao Wang and Hui Yan
Page 1029

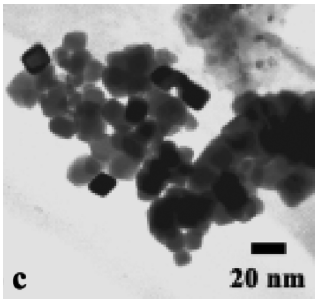

The TEM micrographs and SAED patterns of $Bi_2Sn_2O_7$ powders synthesized by hydrothermal method at 200 °C.

Synthesis, structure and physical properties of $GdCu_4Al$ and $GdCu_4Ga$
Svilen Bobev, Veronika Fritsch, Joe D. Thompson and John L. Sarrao
Page 1035

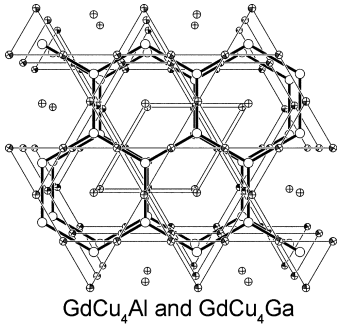

Perspective view of the hexagonal structure of $GdCu_4Al$ and $GdCu_4Ga$ ($CaCu_5$-type), viewed down the *c*-axis.

Directional metal–hydrogen bonding in interstitial hydrides. III. Structural study of $ErCo_3D_x$ ($0 \leqslant x \leqslant 4.3$)
Y.E. Filinchuk and K. Yvon
Page 1041

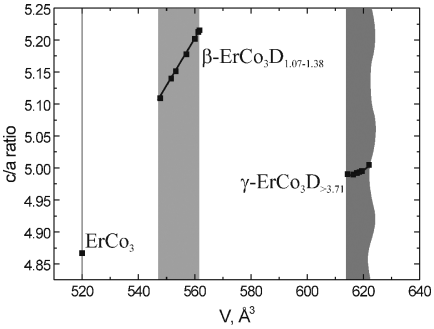

Axial ratio *c*/*a* versus rhombohedral cell volume of $ErCo_3$–deuterium system showing single- and two-phase regions.

Continued

Azine bridged silver coordination polymers: Powder X-ray diffraction route to crystal structure determination of silver benzotriazole

Manju Rajeswaran, Thomas N. Blanton, David J. Giesen, David R. Whitcomb, Nicholas Zumbulyadis, Brian J. Antalek, Marcus M. Neumann and Scott T. Misture

Page 1053

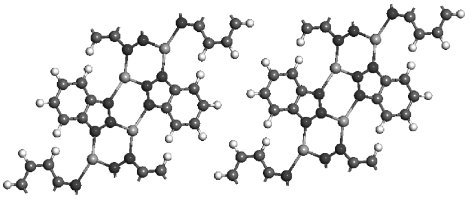

The unit cell packing showing infinite cross-linked chains in the structure of AgBZT.

Thioether moiety functionalization of mesoporous silica films for the encapsulation of highly dispersed gold nanoparticles

Jinlou Gu, Liangming Xiong, Jianlin Shi, Zile Hua, Lingxia Zhang and Lei Li

Page 1060

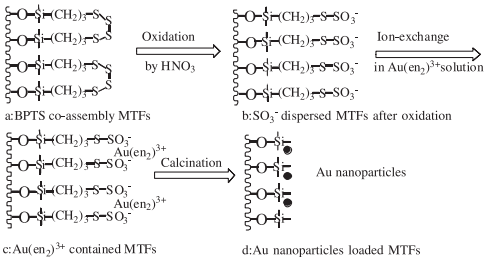

Proposed mechanism for the formation of Au nanoparticles embedded composite films. (a) BPTS co-assembly MTFs, (b) SO_3^- dispersed MTFs after oxidation, (c) $Au(en_2)^{3+}$ contained MTFs, and (d) Au nanoparticles loaded MTFs.

Formation of crystalline $TiO_{2-x}N_x$ and its photocatalytic activity

Jum Suk Jang, Hyun Gyu Kim, Sang Min Ji, Sang Won Bae, Jong Hyeon Jung, Byung Hyun Shon and Jae Sung Lee

Page 1067

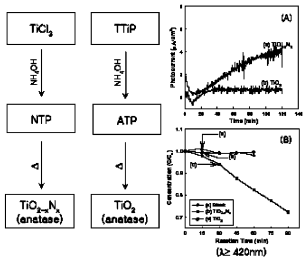

Amorphous precursors to nitrogen-doped TiO_2 (NTP) and pure TiO_2 (ATP) powders were synthesized by hydrolytic synthesis and SGM, respectively. Corresponding crystalline phases were obtained by thermally induced transformation of these amorphous powders. $TiO_{2-x}N_x$ photocatalyst demonstrated its photoactivity for photocurrent generation (A) and decomposition of 2-propanol (B) under visible light irradiation ($\lambda \geqslant 420$ nm).

A-site cation ordering in $AA'BB'O_6$ perovskites

Meghan C. Knapp and Patrick M. Woodward

Page 1076

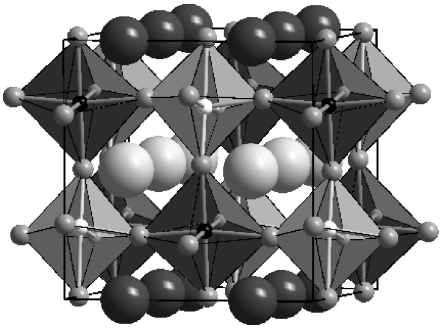

The structure of $NaLaMgWO_6$, a double perovskite with A- and B-site ordering.

Photoluminescent behavior of SrB_4O_7:RE^{2+} (RE = Sm and Eu) prepared by Pechini, combustion and ceramic methods

R. Stefani, A.D. Maia, E.E.S. Teotonio, M.A.F. Monteiro, M.C.F.C. Felinto and H.F. Brito

Page 1086

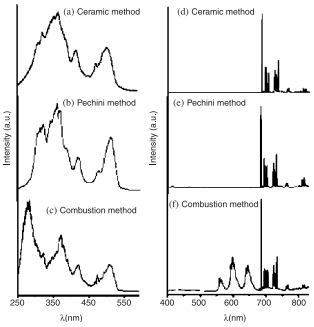

Luminescence spectra of SrB_4O_7:Sm^{2+} system prepared by ceramic, Pechini and combustion methods: (a) excitation spectra recorded with emission monitored around 685 nm and (b) emission spectra recorded under excitation at 350 nm.

High-temperature phase equilibria in the oxide systems $SrFe_{1-x}Ga_xO_{2.5}$–$SrFe_{1-x}Ga_xO_3$ (x = 0, 0.1, 0.2)

I.A. Leonidov, M.V. Patrakeev, J.A. Bahteeva, E.B. Mitberg, V.L. Kozhevnikov, P. Colomban and K.R. Poeppelmeier

Page 1093

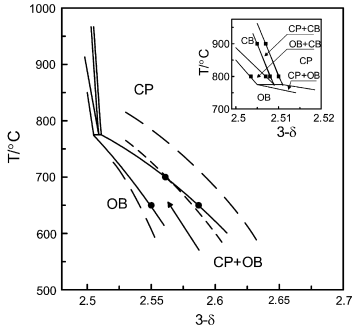

The high-temperature phase diagram for $SrFeO_{3-\delta}$.

Synthesis and phase transition of Li–Mn–O spinels with high Li/Mn ratio by thermo-decomposition of $LiMnC_2O_4$(Ac)

Xin-Cun Tang, Cheng-Kui Jiang, Chun-Yue Pan, Bo-Yun Huang and Yue-Hui He

Page 1100

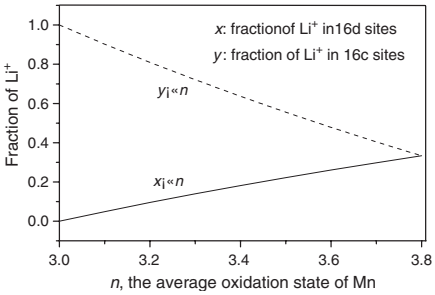

Function of the average oxidation state of Mn with the fraction of Li^+ in the octahedral 16*d* sites ($x \sim n$) and octahedral 16*c* sites ($y \sim n$) for $Li_{1+y}[Mn_{2-x}Li_x]_{16d}O_4$ spinels (Li:Mn = 1, in the case of $2x + y = 1$).

Synthesis of layered zinc hydroxide chlorides in the presence of Al(III)

Tatsuo Ishikawa, Kumi Matsumoto, Kazuhiko Kandori and Takenori Nakayama

Page 1110

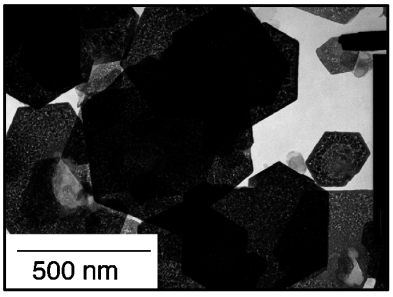

Layered ZHC particles formed at Al/Zn = 0.1.

Nanocrystalline CaF_2 particles obtained by high-energy ball milling

G. Scholz, I. Dörfel, D. Heidemann, M. Feist and R. Stösser

Page 1119

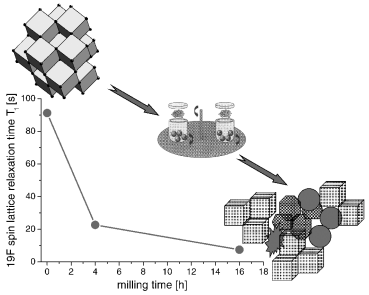

Structural changes in both mechanically treated and mechanochemically synthesized CaF_2 powders have been studied by XRD, TEM, TA, ^{19}F and ^1H MAS NMR and EPR methods. The applied methods indicate that all mechanically treated samples become, under the applied conditions, *nanocrystalline*. The relaxation behavior of both nuclear and electron spins appears to be the most sensitive tool for the investigation of mechanically and chemically induced changes.

Synthesis and adsorption properties of *p*-sulfonated calix[4 and 6]arene-intercalated layered double hydroxides

Satoru Sasaki, Sumio Aisawa, Hidetoshi Hirahara, Akira Sasaki, Hirokazu Nakayama and Eiichi Narita

Page 1129

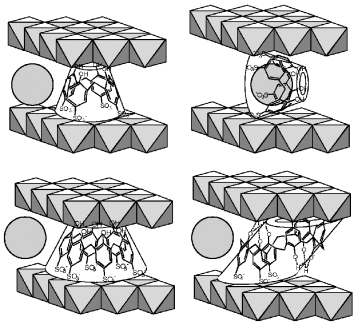

Schematic representation of CS oriented in interlayer space of LDH.

Structural and magnetic properties of the Kagomé antiferromagnet $YbBaCo_4O_7$

A. Huq, J.F. Mitchell, H. Zheng, L.C. Chapon, P.G. Radaelli, K.S. Knight and P.W. Stephens

Page 1136

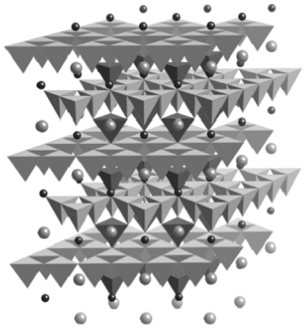

Crystal structure of $YbBaCo_4O_7$ at 225 K showing tetrahedral coordination polyhedra surrounding both Co^{2+} and Co^{3+} ions and highlighting the Kagomé layers. At this temperature, the structure is trigonal and geometrically frustrated.

Preparation and characterization of microporous SiO_2–ZrO_2 pillared montmorillonite

Yang-Su Han and Shoji Yamanaka

Page 1146

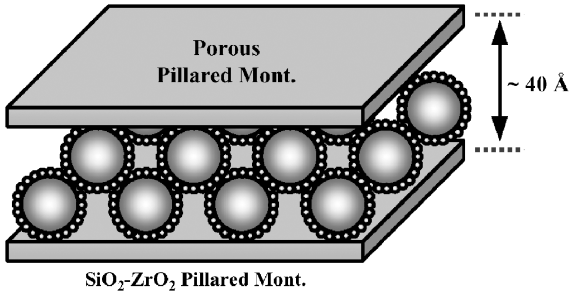

Schematic structural model of SiO_2–ZrO_2 pillared montmorillonite.

Continued

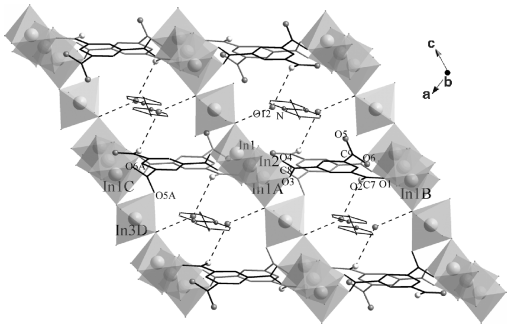

Four In(III)-btc isostructural polymers with 3-D channel frameworks formed from octahedral chain-like sinusoidal curves and layers interlinking. The guests pyridine and its derivatives at channels can be exchanged by K^+, Sr^{2+} and Ba^{2+} ions.

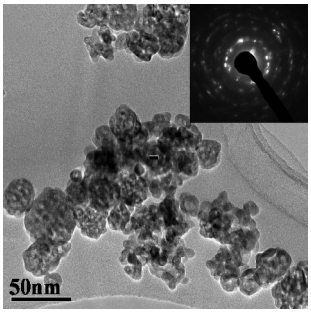

HRTEM images of the 1 mol% cerium-doped TiO_2 nanoparticles calcined at 300 °C.

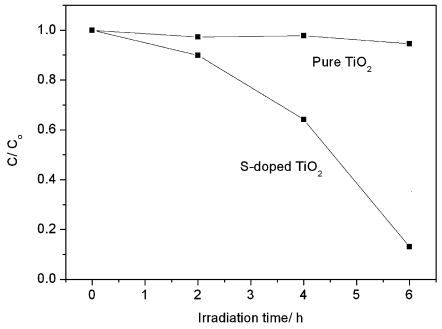

A one-step low-temperature hydrothermal route was developed for the synthesis of S-doped TiO_2 photocatalysts from TiS_2 and HCl.

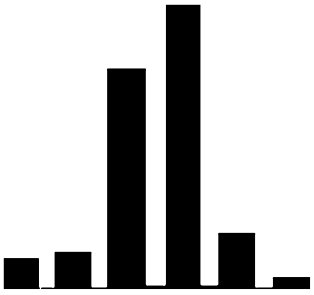

Distributions of acentric niobates and tantalates over crystal systems.

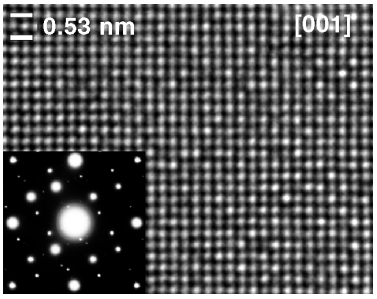

The cation-deficient $Ag_{1/8}Pr_{5/8}MoO_4$ phase exhibits an incommensurate modulation that can be interpreted by means of transmission electron microscopy and X-ray diffraction as an occupancy modulation where one-fourth of the Ag/Pr atoms are absent. The crystal structure of $Ag_{1/8}Pr_{5/8}MoO_4$ is refined from X-ray powder diffraction data.

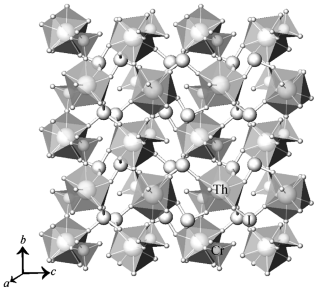

A view of the chiral three-dimensional structure of $Th(CrO_4)(IO_3)_2$.

Pressure-induced structural changes of the tetragonal Bi_2CuO_4

F.X. Zhang, B. Manoun, S.K. Saxena and C.S. Zha

Page 1202

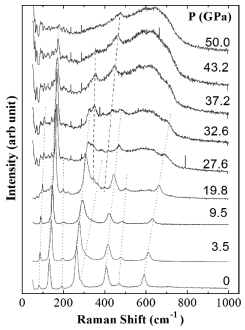

Raman spectrum evolution with pressure clearly indicates a pressure-induced structural transition occurred in Bi_2CuO_4 at pressures above 20 GPa.

Decoration of carbon nanotubes with iron oxide

Cao Huiqun, Zhu Meifang and Li Yaogang

Page 1208

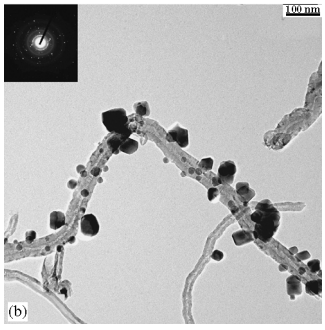

TEM images of MWNTs decorated with iron oxide nanoparticles.

A generic method of visible light sensitization for perovskite-related layered oxides: Substitution effect of lead

Hyun G. Kim, Olav S. Becker, Jum S. Jang, Sang M. Ji, Pramod H. Borse and Jae S. Lee

Page 1214

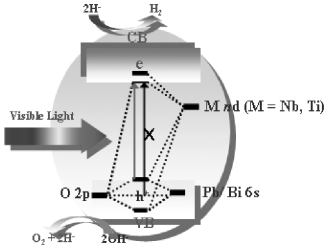

Schematic band energy diagram of lead-substituted perovskite-related oxides.

Ab initio structure determination of novel borate $NaSrBO_3$

L. Wu, X.L. Chen, Y. Zhang, Y.F. Kong, J.J. Xu and Y.P. Xu

Page 1219

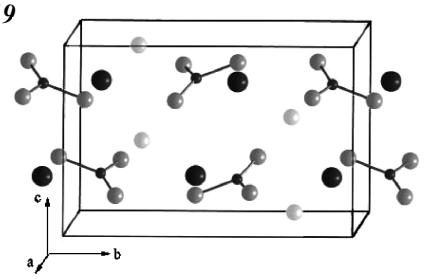

A novel orthoborate, $NaSrBO_3$, has been successfully synthesized by standard solid-state reaction, and the crystal structure has been determined from powder X-ray diffraction data. It crystallizes in the monoclinic space group $P2_1/c$ with lattice parameters: $a = 5.32446(7)$ Å, $b = 9.2684(1)$ Å, $c = 6.06683(8)$ Å, $\beta = 100.589(1)$. The fundamental building units are isolated BO_3 groups. The infrared spectrum and a comparison of the new structure type with the other known orthoborates are also discussed.

Low temperature synthesis of Mn_3O_4 polyhedral nanocrystals and magnetic study

Li-Xia Yang, Ying-Jie Zhu, Hua Tong, Wei-Wei Wang and Guo-Feng Cheng

Page 1225

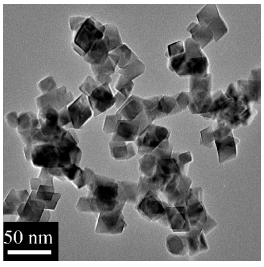

Manganese oxide (hausmannite) polyhedral nanocrystals were prepared by a microwave-assisted solution-based method using $Mn(CH_3COO)_2$ and $(CH_2)_6N_4$ at 80 °C. Mn_3O_4 polyhedral nanocrystals prepared by microwave heating at 80 °C for 60 min were of cubic and rhombohedral shapes with the edge lengths in the range of 15–40 nm. The magnetic behavior of Mn_3O_4 nanocrystals was studied.

Solvothermal synthesis and removal capacity for hydrogen chloride gas of $Zn(OH)(NO_3)$ with a rare (10,3)-*d* net

Jinyu Sun, Yaming Zhou, Zhenxia Chen, Guangshan Zhu, Qianrong Fang, Rongjing Yang, Shilun Qiu and Dongyuan Zhao

Page 1230

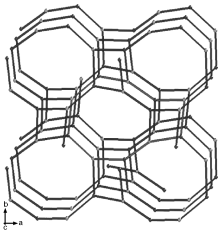

A paradigm of 10,3-*d* net.

Continued

Defect generation of rutile-type SnO_2 nanocondensates: Imperfect oriented attachment and phase transformation
Wan-Ju Tseng, Pouyan Shen and Shuei-Yuan Chen
Page 1237

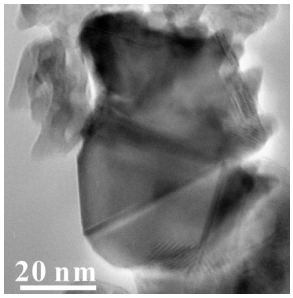

Lattice image of rutile-type SnO_2 nanocondensates with {110} and {101} faces in [111] zone axis, which were coalesced over a specific $(10\bar{1})$ contact plane to form twinned bicrystals.

Formation of star-shaped calcite crystals with Mg^{2+} inorganic mineralizer without organic template
Liying Zhu, Qingrui Zhao, Xiuwen Zheng and Yi Xie
Page 1247

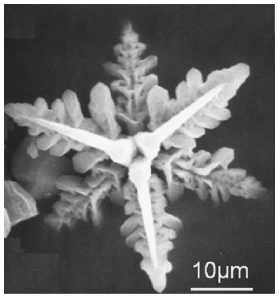

Star-shaped calcite crystals with $\bar{3}m$ symmetry were obtained in the mixed solvent of ethanol and H_2O (4:1 vol%) using Mg^{2+} as grow mineralizer without any organic template under the solvothermal condition. The star-shaped crystals branched to the six directions perpendicular to the *c*-axis. In the process, Mg^{2+} ions and the solvent play very important roles in the formation of the star-shaped calcite and the formation process was also primarily studied.

Novel method for the preparation of core–shell nanoparticles with movable Ag core and polystyrene loop shell
Wei-Jun Liu, Zhi-Cheng Zhang, Wei-Dong He, Cheng Zheng, Xue-Wu Ge, Jian Li, Hua-Rong Liu and Hao Jiang
Page 1253

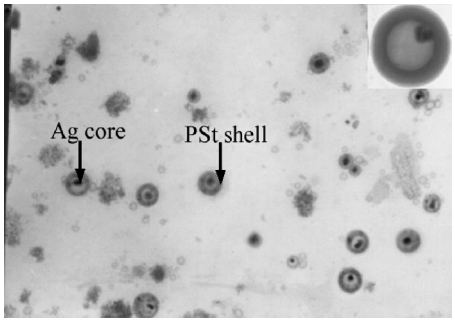

TEM image of Ag@PSt hybrid nanoparticles.

The evolution of structural changes in ettringite during thermal decomposition
Michael R. Hartman, Steven K. Brady, Ronald Berliner and Mark S. Conradi
Page 1259

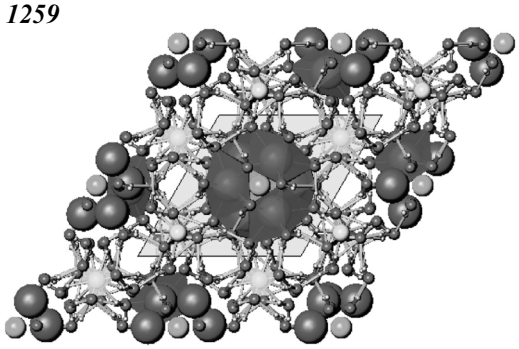

A $2 \times 2 \times 2$ unit cell configuration of ettringite as viewed down the *c*-axis. Changes within the ettringite structure were observed during the thermal decomposition of the material, revealing extensive changes in the bonding structure of the material.

Mixed conductivity and Mössbauer spectra of $(La_{0.5}Sr_{0.5})_{1-x}Fe_{1-y}Al_yO_{3-\delta}$ ($x = 0$–0.05, $y = 0$–0.30)
Vladislav V. Kharton, Joao C. Waerenborgh, Alexander P. Viskup, Sergey O. Yakovlev, Mikhail V. Patrakeev, Piotr Gaczyński, Ivan P. Marozau, Aleksey A. Yaremchenko, Aliaksandr L. Shaula and Victor V. Samakhval
Page 1273

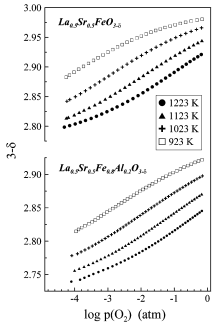

Oxygen nonstoichiometry of perovskite-type (La,Sr) (Fe,Al)$O_{3-\delta}$.

Mesoporous hybrid organosilica containing urethane moieties
You-Kyong Seo, Sung-Bae Park and Dong Ho Park
Page 1285

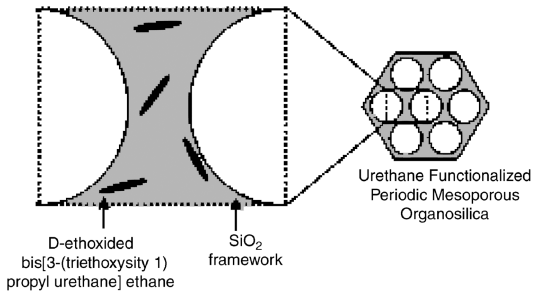

Mesoporous hybrid material containing urethane moieties in functionalized long chain organic group have been synthesized by using bis[3-(triethoxysilyl) propyl urethane]ethane (BTESPUE) and tetraethoxysilane as structural ingredients.

Superconductivity in $Li_3Ca_2C_6$ intercalated graphite
Nicolas Emery, Claire Hérold, Jean-François Marêché, Christine Bellouard, Geneviève Loupias and Philippe Lagrange
Page 1289

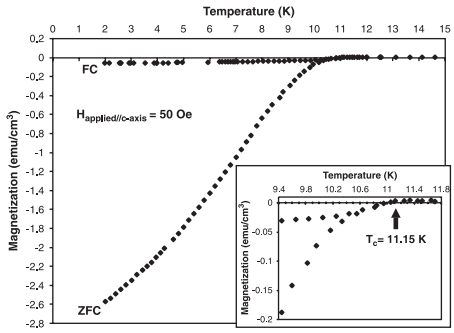

Magnetisation of $Li_3Ca_2C_6$ versus temperature with a 50 Oe field applied parallel to the *c*-axis (field cooling FC, and zero field cooling ZFC measurements).

Corrigendum to "Subsolidus phase relations in Na_2O–CuO–Sb_2O_n system and crystal structure of new sodium copper antimonate $Na_3Cu_2SbO_6$" [J. Solid State Chem. 178 (2005) 1165–1170]
O.A. Smirnova, V.B. Nalbandyan, A.A. Petrenko and M. Avdeev
Page 1293

NOTICE

The Keyword Index for Volume 179 will appear in the December 2006 issue as part of a cumulative index for the year 2006.